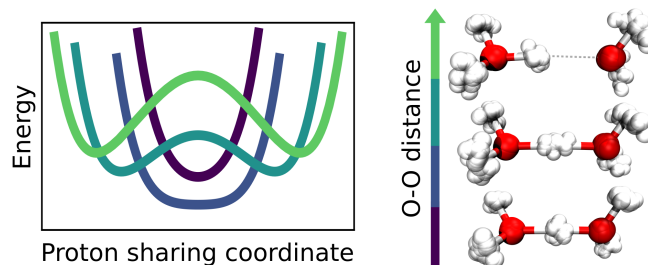


Converged Colored Noise Path Integral Molecular Dynamics Study of the Zundel Cation down to Ultra-low Temperatures at Coupled Cluster Accuracy

Christoph Schran,^{1, a)} Fabien Briec,^{1, a)} and Dominik Marx¹
Lehrstuhl für Theoretische Chemie, Ruhr-Universität Bochum, 44780 Bochum, Germany

(Dated: March 25, 2021)

For a long time, performing converged path integral simulations at ultra-low, but finite temperatures of a few Kelvin has been a nearly impossible task. However, recent developments in advanced colored noise thermostating schemes for path integral simulations, namely the Path Integral Generalized Langevin Equation Thermostat (PIGLET) and the Path Integral Quantum Thermal Bath (PIQTB), have been able to greatly reduce the computational cost of these simulations, thus making the ultra-low temperature regime accessible in practice. In this work, we investigate the influence of these two thermostating schemes on the description of hydrogen-bonded systems at temperatures down to a few Kelvin as encountered, for example, in helium nanodroplet isolation or tagging photodissociation spectroscopy experiments. For this purpose, we analyze the prototypical hydrogen bond in the Zundel cation (H_5O_2^+) as a function of both, oxygen-oxygen distance and temperature in order to elucidate how the anisotropic quantum delocalization and, thus, the shape of the shared proton adapts depending on the donor-acceptor distance. The underlying electronic structure of the Zundel cation is described in terms of Behler’s Neural Network Potentials of essentially converged Coupled Cluster accuracy, CCSD(T*)-F12a/AVTZ. In addition, the performances of the PIQTB and PIGLET methods for energetic, structural, and quantum delocalization properties are assessed and directly compared. Overall, our results emphasize the validity and practical usefulness of these two modern thermostating approaches for path integral simulations of hydrogen-bonded systems even at ultra-low temperatures.



Keywords: Zundel Cation, Hydrogen Bonds, Ultra-low Temperatures, Path Integrals, Colored Noise Thermostating

I. INTRODUCTION

Experimental techniques operating at ultra-low temperatures such as helium nanodroplet isolation^{1–3} and tagging photodissociation^{4,5} spectroscopy experiments have provided many insights on the nature and properties of fragile molecules and clusters that cannot be studied in the gas phase on their own. Computational studies complement these experiments and help elucidating some of the microscopical mechanisms at work as, for example, shown for the dissociation of microsolvated HCl/water clusters^{6,7} or understanding of proton transfer in protonated water clusters.⁸ However, at these ultra-low temperatures, nuclear quantum effects (NQEs), such as quantum delocalization due to zero-point motion and tunneling need to be taken into account, if qualitative or even quantitative conclusions are of interest. In such cases, simulation techniques based on the path integral (PI) formalism of quantum mechanics, such as PI molecular dynamics (PIMD),^{9–11} are a

reliable tool to explicitly include NQEs. These methods use the discretized imaginary time path integral formulation of the quantum partition function allowing, in principle, to obtain the exact quantum thermodynamic properties of the system.^{12–14} In practice, properties converge towards their exact quantum values when the discretization of the path integral P (usually called number of replicas, beads or Trotter index) is large enough. However, the number of replicas to reach this convergence increases unfavorably upon lowering the temperature, thus making it especially complicated to treat systems at temperatures of a few Kelvin. A wealth of different methods have been proposed to accelerate PIMD simulations that are based on distinct approaches such as higher-order Trotter discretization schemes,^{15–20} actions based on the pair density matrix,^{14,21} ring polymer contractions,^{22–25} or colored noise thermostating^{26,27} as well as post-processing or reweighting schemes^{28–30} to name but a few. Among these approaches, the use of colored noise thermostats is able to significantly reduce the number of replicas required to reach the convergence of PIMD simulations^{26,27} which is necessary if one wants to reach ultra-low temperatures.³¹ In particular, it has been shown that the Path Integral Gener-

^{a)}These authors contributed equally.

alized Langevin Equation Thermostat (PIGLET),³² can be used to accelerate the convergence by around two orders of magnitude even in the complicated case of the highly fluxional and thus utmost anharmonic protonated methane molecule (CH_5^+) at ultra-low temperature.³¹ Another colored noise thermostating scheme to accelerate PIMD simulations, based on the same principle as PIGLET but using a different colored noise thermostat, called Path Integral Quantum Thermal Bath (PIQTB), has recently been developed.²⁷ However, the performance of this method at ultra-low temperatures as well as its comparison to PIGLET simulations remain unknown up to now.

In the present work we systematically scrutinize these two colored noise thermostating schemes by studying NQEs on the prototypical hydrogen bond in the Zundel cation^{33,34} as a function of temperature down to the order of one Kelvin. Moreover, varying the donor-acceptor distance with the help of suitable restraints allows us to continuously transform a strong and centered hydrogen bond to a weak and very asymmetric one. This enables us to quantify if and to which extent PIGLET and PIQTB artificially change the shape of nuclei that are subject to anisotropic quantum delocalization, such as protons in hydrogen bonds of different length. For this purpose, we analyze how the PIGLET and PIQTB methods perform for various energetic, structural and quantum delocalization properties, thus for the first time comparing these two methods directly with respect to standard PIMD simulations that have been converged by using very large replica numbers P .

The outline of the paper is as follows: We first describe the relevant aspects of the methodology with a focus on the similarities and differences of PIGLET and PIQTB in Sec. II and provide the computational details in Sec. III. In the first two parts of Sec. IV, we compare the path integral convergence of energetic and structural properties of the Zundel cation. Afterwards, delocalization properties are addressed in the last two parts of Sec. IV where we investigate, in particular, the convergence of the quantum delocalization and, in order to draw some general conclusions, the anisotropy of this delocalization as a function of the heavy atom distance. Finally, we conclude and suggest some directions for future work.

II. METHODS: ACCELERATED PATH INTEGRAL MOLECULAR DYNAMICS

Although stochastic thermostating has a long tradition in PIMD to render sampling of the path integral ergodic, stochastic thermostats using colored noise have been explored only fairly recently. Initially, these colored noise methods have been developed to efficiently emulate NQEs in standard MD simulations, thus avoiding the computationally much more demanding PIMD simulations altogether. Two different underlying principles have been exploited to this end, namely the Generalized

Langevin Equation (GLE)³⁵ and the Quantum Thermal Bath (QTB).³⁶ The main idea behind both of these approaches is to achieve a frequency-dependent thermalization of the system so that the average energy of a vibrational mode of angular frequency ω ,

$$\langle E(\omega) \rangle = \frac{\hbar\omega}{2} \coth\left(\frac{\beta\hbar\omega}{2}\right), \quad (1)$$

is given by the exact quantum expression in the harmonic approximation. In the GLE case, this is achieved using the generalized Langevin equation rewritten in a Markovian form by introducing a set of additional degrees of freedom (DoFs) that represents the quantum bath.^{37,38} Although the equations of motion are then Markovian, the coupling between the physical and the additional DoFs leads to a non-Markovian process for the physical variables.^{37,38} The introduction of these additional DoFs allows for great flexibility so that the GLE can actually be used for different purposes such as optimal sampling,³⁹ selective normal mode excitation^{40,41} and, of course, frequency-dependent thermostating^{35,41} in particular to include NQEs. However, this flexibility comes at the price of a large number of parameters which need to be carefully optimized in order to accurately reproduce the energy distribution of Eq. (1). This is done, in practice, using a highly complex and non-trivial fitting procedure to parameterize the GLE approach.³⁷

In the QTB case, the target energy distribution is enforced using a modified Langevin thermostat where the Gaussian white noise is replaced by a colored noise.³⁶ The standard Langevin thermostat introduces a friction force, with a friction coefficient γ , and a random force R so that the equation of motion for a DoF i is given by the Langevin equation,

$$\dot{p}_i = -\nabla_i V(\{q\}) - \gamma p_i + \sqrt{2m_i\gamma} R_i. \quad (2)$$

In the case of usual classical nuclear dynamics at constant temperature T , the random force is a Gaussian white noise whose power spectral density I_{R_i} is given by the classical fluctuation-dissipation theorem⁴² and is equal to the thermal energy $k_B T$ so that the autocorrelation function of R_i satisfies

$$\langle R_i(t) R_i(t + \tau) \rangle = k_B T \delta(\tau). \quad (3)$$

In the QTB case, the Gaussian white noise is replaced by a colored noise which thus has a frequency-dependent power spectral density $I_{R_i}(\omega)$ that is equal to the target energy distribution $\langle E(\omega) \rangle$ of Eq. (1) according to the quantum fluctuation-dissipation theorem as formulated by Callen and Welton.⁴³ The autocorrelation function of R_i ,

$$\langle R_i(t) R_i(t + \tau) \rangle = \int_{-\infty}^{\infty} I_{R_i} e^{-i\omega\tau} d\omega, \quad (4)$$

is then obtained using the Wiener-Khinchin theorem. One very appealing aspect of the QTB is its relative simplicity compared to the GLE thermostat. Indeed, the

method only depends on a few parameters and relies on a simple Langevin thermostat that is easy to implement and is already available in most MD codes. In practice, one only needs to generate random forces having the correct power spectrum which can easily be done on-the-fly using a moving average (or finite impulse response, FIR) filter as proposed earlier.⁴⁴

Both the QTB and GLE methods are able to include part of the quantum effects, such as zero-point energy, in a computationally inexpensive way and have been successfully applied to various systems.^{45–53} However, the use of these thermostats is restricted to weakly anharmonic systems. Indeed, the energy distribution of Eq. (1) is formally valid in the harmonic case only, but the main limitation of these methods in anharmonic cases is that they are prone to the problem of zero-point energy leakage (ZPEL). Due to anharmonic couplings between the normal modes, part of the energy is transferred from the high frequency modes to the low frequency ones, leading to the wrong energy distribution.^{37,54–56} Even though it is possible to limit the effect of ZPEL by enforcing a strong coupling between the system and the thermostat,^{37,56} it is impossible to know how accurate the obtained results are when studying unknown systems.

Beyond approximately including NQEs in a classical MD framework via thermostatting, these two colored noise schemes have been shown to be particularly useful in combination with PIMD, where ergodic thermostatting is fundamentally required.¹¹ Within the PIMD framework, GLE- and QTB-based methods can be systematically converged towards the exact results by increasing the number of beads.^{26,27} Parts of the NQEs are already included via the thermostat, which implies immediately that less replicas compared to canonical PIMD simulations are required to reach convergence.^{26,27} Thus, the use of colored noise thermostats is able to greatly accelerate the convergence of standard PIMD.^{26,27}

In the framework of accelerating Trotter convergence of PIMD simulations, the main idea of colored noise thermostats remains to achieve a frequency-dependent thermalization of the system to impose the right quantum energy distribution in the harmonic approximation. However, this energy distribution now applies to all the normal modes of the ring polymer and depends on the number of replicas P used in the PIMD simulation. Let us consider the simple case of a one dimensional harmonic oscillator of angular frequency ω . Its average energy can be expressed as

$$\langle E(\omega) \rangle_P = \frac{1}{P} \sum_{k=1}^P \frac{\omega^2}{\omega_k^2} \langle \tilde{E}(\omega_k) \rangle_P, \quad (5)$$

where $\langle \tilde{E}(\omega_k) \rangle_P$ is the average energy of the ring polymer normal mode k of angular frequency ω_k ; here $\omega_k^2 = \omega^2 + 4\omega_p^2 \sin^2((k-1)\pi/P)$ with $k = 1, \dots, P$. In the standard PIMD case, the ring polymer is classically thermalized at the temperature $T \times P$, so that $\langle \tilde{E}(\omega_k) \rangle_P = k_B T \times P$. When the number of replicas P increases, the average

energy of the harmonic oscillator converges towards its exact quantum value given by Eq. (1). Colored noise thermostats can be used in order to ensure that $\langle E(\omega) \rangle_P$ is given by the exact quantum expression for any value of P . This is achieved by enforcing an energy distribution $\langle \tilde{E}(\omega_k) \rangle_P$ among the ring polymer normal modes that is the solution of the following equation

$$\frac{1}{P} \sum_{k=1}^P \frac{\omega^2}{\omega_k^2} \langle \tilde{E}(\omega_k) \rangle_P = \frac{\hbar\omega}{2} \coth\left(\frac{\beta\hbar\omega}{2}\right), \quad (6)$$

which is directly obtained by combining Eqs. (1) and (5). This equation can be solved numerically for any values of P and the obtained energy distribution $\langle \tilde{E}(\omega_k) \rangle_P$ can then be enforced using either the GLE thermostat, leading to the PIGLET method,^{26,32} or the QTB, leading to the PIQTB method.²⁷ In the latter case, each ring polymer normal mode is submitted to a random force that is a colored noise whose power spectral density is the target energy distribution $\langle \tilde{E}(\omega_k) \rangle_P$ in the same spirit as in plain QTB. Both methods are able to include part of the quantum fluctuations (mostly the harmonic part) via the thermostat so that the number P of replicas required to Trotter-converge the PIMD simulation is significantly reduced.

For PIGLET, we refer to a recent publication³¹ concerning its details and implementation in the CP2k program package^{57,58} as well as its performance assessment in the realm of ultra-low temperature simulations, whereas the PIQTB technique as such and its implementation in CP2k are described in Sec. I of the Supporting Information.

III. COMPUTATIONAL DETAILS

All simulations have been carried out using the CP2k simulation package.^{57,58} In particular, the standard PIMD reference simulations (where Trotter convergence is achieved by using very large P values) have been carried out using the standard path integral Langevin equation (PILE) thermostat⁵⁹ with a friction parameter for the centroid mode of $\gamma = 1 \text{ ps}^{-1}$ whereas the friction coefficients for the other modes are given by $\gamma_k = \tilde{\omega}_k$ with $k = 2, \dots, P$ where $\tilde{\omega}_k$ are the usual angular frequencies of the free particle ring polymer normal modes given by $\tilde{\omega}_k = 2\omega_p \sin((k-1)\pi/P)$. In terms of CP2k parameters this setup corresponds to $\tau = 1000 \text{ fs}$ and $\lambda = 0.5$. The PIGLET simulations have been performed using the matrices (containing all the GLE parameters) as developed in Ref. 31 to study CH_5^+ at ultra-low temperatures. For PIGLET, we are thus limited to a maximum of $P = 32, 64$ and 512 beads at $T = 100, 20$ and 1.67 K , respectively.

The PIQTB method has been implemented by us into the CP2k simulation package. In the same spirit as for the PILE thermostat, every ring polymer normal mode is coupled to its own QTB thermostat except for the centroid ($k = 1$) mode which is attached to a classical

Langevin thermostat. The value of the friction coefficient of the centroid normal mode is set to $\gamma = 20 \text{ ps}^{-1}$ and the friction coefficients for the other modes ($k = 2, \dots, P$) are scaled so that $\gamma_k^2 = \gamma^2 + \lambda^2 \tilde{\omega}_k^2$ with $\lambda = 0.2$. The angular cutoff frequency we use for the centroid mode is $\omega_{\text{cut},1} = 1100 \text{ rad ps}^{-1}$ and the cutoff frequencies for the other modes are scaled so that $\omega_{\text{cut},k}^2 = \omega_{\text{cut},1}^2 + \lambda_{\text{cut}}^2 \tilde{\omega}_k^2$ with $\lambda_{\text{cut}} = 1.5$. In terms of CP2k parameters this setup corresponds to $\tau = 50 \text{ fs}$, $\lambda = 0.2$, $\tau_{\text{cut}} = 0.9 \text{ fs}$ and $\lambda_{\text{cut}} = 1.5$. In the following, all kinetic energies using PIQTB thermostating are obtained using the modified virial estimator introduced in Ref. 27. More details about the implementation of PIQTB in CP2k, the choice of the parameters and the kinetic energy estimator are given in the Supporting Information. All reported PI simulations were propagated for 0.5 ns using a formal molecular dynamics timestep of 0.25 fs where 10 ps at the beginning of each simulation were discarded as equilibration from the starting configuration.

The electronic structure of the Zundel cation is in principle accessible up to Coupled Cluster theory by on-the-fly electronic structure calculations as impressively shown in the pioneering study of Ref. 34 made possible due to modern Car-Parrinello-like approaches.⁶⁰ However, full convergence of the electronic structure and path integral discretization, especially at ultra-low temperatures, are still out of scope for these approaches. Energies and forces of the Zundel cation were, therefore, obtained using a Neural Network Potential^{61,62} fitted to CCSD(T*)-F12a/AVTZ reference data that has been developed similarly as described in Ref. 63. As demonstrated in the Supplemental Material therein,⁶³ this machine learning approach provides electronic-structure-based interactions and thus the global potential energy surface (PES) of the protonated water dimer at the essentially converged Coupled Cluster level. This allows us similarly as recently demonstrated for a different machine learning technique⁶⁴ to run electronically converged simulations at the gold standard of modern quantum chemistry.

In order to systematically investigate the response of the shape of the proton in the hydrogen bond with respect to the intermolecular distance, the symmetric Zundel complex $[\text{H}_2\text{O} \cdots \text{H} \cdots \text{OH}_2]^+$ was restrained by applying two identical external three-dimensional isotropic harmonic potentials that exclusively act on every bead of the two oxygen atoms in the laboratory fixed coordinate system. After careful testing, the spring constants of the two harmonic potentials were set to $0.5 E_h a_0^{-2}$ to enforce the desired heavy atom separation while still allowing for sufficient fluctuations. If not specified differently, the shared proton was initialized between the oxygen atoms using the OH distance of the equilibrium structure, thus closer to one of the oxygen atoms for the larger O-O separations. Note that the respective observables in the next section are reported as a function of the resulting quantum expectation value of the donor-acceptor distance, being the average oxygen-oxygen distance $\langle r_{\text{OO}} \rangle$ as obtained from the PI simulations, at the

given temperature.

IV. RESULTS AND DISCUSSION

In the following we carry out a detailed comparison of the performance of the PIQTB and PIGLET methods to study the Zundel cation down to ultra-low temperatures. In the first two parts, we focus on the convergence behavior of the two methods as compared to standard PIMD for several quantities of interest such as average energies and selected structural properties. Then, in the last two parts, we study systematically the impact of these thermostats on the delocalization properties of the atoms and, in particular, of the shared proton as a function of the hydrogen bond length.

A. Energetic Properties

As mentioned above, colored noise thermostats have been designed to speed up the convergence of PIMD simulations targeting specifically the convergence of the average kinetic and potential energies. We thus start here by comparing the convergence of these average energies with respect to the number of path integral replicas P as obtained from PILE, PIGLET and PIQTB simulations of the Zundel cation at 100, 20 and finally 1.67 K which is depicted in Fig. 1. Starting from classical MD simulations (obtained from PILE simulations in the $P = 1$ limit), increasing the number of path integral replicas in the canonical PILE simulations leads to a monotonic increase of the average energies that finally converges to a constant plateau value equal to the quantum average energy.

As expected, the number P of beads required to reach this convergence limit increases drastically when the temperature is decreased; note the logarithmic P scale in Fig. 1. In case of the PILE thermostat, around 128 replicas are necessary at 100 K, while at 20 K, a Trotter number of approximately $P = 512$ is needed. Finally, at 1.67 K, one needs to use at least 4096 replicas in order to reach convergence. This is a clear illustration of the limitation of standard PIMD to study systems at such ultra-low temperatures. Additionally, one can see that the converged energies are basically constant with temperature indicating that the system is almost in its ground state already at 100 K. Thus the main contribution to the energies comes from zero-point energy whereas the thermal fluctuations are negligible compared to the quantum ones at all temperatures that we address in the present investigation.

The use of colored noise thermostats is clearly accelerating the convergence of the energies as seen in Fig. 1. Indeed, the average energies obtained by PIQTB and PIGLET are very close to their converged values even for rather low values of P . This is particularly striking for the PIQTB method at 1.67 K where the energies

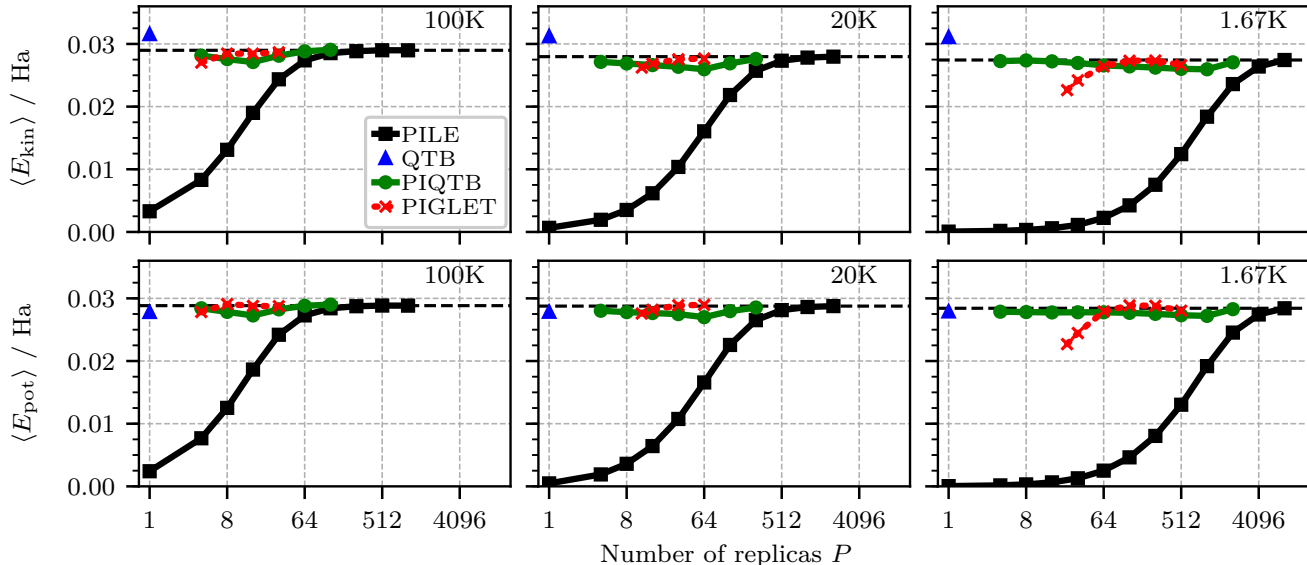


Figure 1. Convergence of the average kinetic (top) and potential (bottom) energies of the Zundel cation, H_5O_2^+ , with respect to the number of replicas P at $T = 100, 20$ and 1.67K as obtained using the PILE (black squares), PIGLET (red crosses) and PIQTB (green circles) thermostats. The blue triangles show the energies obtained with the bare QTBT ($P = 1$) thermostat, which corresponds to a classical MD simulation with QTBT colored noise thermostating. The potential energies presented here are given relative to the potential energy of the equilibrium structure of H_5O_2^+ . Note that the statistical error bars as obtained from block averaging are smaller than the symbol size in all shown cases.

are already equal to the converged PILE results for P as low as 4. However, as it has already been shown for the PIGLET thermostat,³¹ the convergence of these methods can exhibit a non-monotonic behavior. Here, this is especially noticeable in the PIQTB case at all three temperatures where a small kink is present in the convergence of the energies that shifts to higher values of P when the temperature is lowered.

The PIGLET method exhibits this behavior only at 1.67K , where we obtain average energies for $P = 512$ that are lower than the ones obtained for $P = 256$. Note that due to the complicated construction of the PIGLET matrices we are limited to 512 replicas at 1.67K for PIGLET, while the number of replicas for PIQTB can continuously be changed without difficulty. The origin of this non-monotonic convergence is not totally clear but, as already discussed in Ref. 31, is most probably related to ZPEL. In any case, the overall convergence behavior of both PIQTB and PIGLET is rather similar and we can see that both methods are very close to the converged value for almost every number of beads, showing that these thermostats are significantly improving the convergence of both, the kinetic and potential energy even down to ultra-low temperatures. Let us also note that even the bare QTBT method (*i.e.* PIQTB for $P = 1$) is already giving quite reliable energy estimates even though it tends to systematically overestimate the kinetic energy. Since both methods have been specifically designed in order to accelerate the convergence of the average energies, the

next step is to investigate how they perform for other physically relevant quantities such as structural observables.

B. Structural Properties

Next, we focus on the molecular structure of the Zundel cation and study in particular the distribution of three selected observables: the OH distance between the dangling hydrogen atoms and their closest oxygen atom, r_{OH} , the hydrogen bond angle between the shared proton and the two oxygens, \angle_{OHO} , and the proton sharing (or proton transfer) coordinate $\delta = r_{\text{O}_1\text{H}} - r_{\text{O}_2\text{H}}$ with $r_{\text{O}_1\text{H}}$ and $r_{\text{O}_2\text{H}}$ being the distance between the shared proton and oxygen O_1 and O_2 , respectively. In order to both, reliably and quantitatively study the convergence of the different observables x , we need to compare the entire distribution functions $\rho_P(x)$ obtained for a certain value of P to the converged one, $\rho(x) = \lim_{P \rightarrow \infty} \rho_P(x)$, obtained with the PILE thermostat using the largest number of beads. We chose to perform this comparison by computing the distance between ρ_P and ρ using a simple metric

$$d(\rho_P, \rho) = \frac{\int_{-\infty}^{+\infty} |\rho_P(x) - \rho(x)| dx}{\int_{-\infty}^{+\infty} \rho_P(x) dx + \int_{-\infty}^{+\infty} \rho(x) dx} \quad (7)$$

based on the absolute difference of the two distributions normalized to a maximum distance of unity. The interested reader can find all distributions for r_{OH} distances,

the \angle_{OHO} angle and the δ coordinate along with distributions of a few more quantities in the Supporting Information.

The convergence of the three distributions is compiled in Fig. 2 by showing the distance $d(\rho_P, \rho)$ as a function of P . In contrast to what has been found for the energies, the distributions of these structural observables converge more slowly to the $P \rightarrow \infty$ quantum distribution even when using PIGLET or PIQTB, yet improved convergence is observed as before considering that a distance of $d(\rho_P, \rho) \approx 1 - 3\%$ corresponds to statistically identical distributions. Yet, much higher bead numbers are necessary for the PILE thermostat to reach convergence in particular when the temperature is low. The convergence behavior of PIGLET and PIQTB follows a similar dependence as PILE, but starts much closer to the converged results for small numbers of replicas; note the double-logarithmic scale in this figure. As seen for the PILE thermostat, the number of beads necessary to reach convergence increases when the temperature decreases, but the convergence of PIQTB and PIGLET becomes especially slow when reaching ultra-low temperatures. For example, increasing P up to 512 has almost no effect on the convergence of the r_{OH} distribution for PIQTB and PIGLET at 1.67 K. Nevertheless, for the distribution of OH distances and the hydrogen bond angle, the use of colored noise thermostats clearly accelerates the convergence as compared to PILE even down to ultra-low temperatures, see Fig. 2. Thus, a great gain in accuracy is already obtained compared to standard PIMD when using a surprisingly small bead number in either PIGLET or PIQTB, whereas ultimate convergence toward the $P \rightarrow \infty$ quantum limit sets in only at unpleasantly large Trotter numbers, in particular at low temperatures.

In case of the proton sharing coordinate δ , however, both PIQTB and PIGLET seem to have great difficulties to converge to the exact result according to the right column in Fig. 2. This behavior is due to the fact that the potential associated with the δ coordinate is highly anharmonic. The top panel of Fig. 4 depicts cuts of the Coupled Cluster PES of H_5O_2^+ showing the potential energy profile along the proton sharing coordinate for different fixed values of the oxygen distance r_{OO} . In our case, the average oxygen distance turns out to be $\langle r_{\text{OO}} \rangle \approx 2.415 \text{ \AA}$ for all temperatures studied here and one can see that the associated energy profile resembles a flat quartic potential at the corresponding value of $r_{\text{OO}} = 2.4 \text{ \AA}$. Highly anharmonic potentials such as the pure quartic well are one of the most difficult cases for accelerated colored noise thermostats since the harmonic term is completely absent.^{65,66} It is thus not surprising that these thermostats show such a slow convergence of the distribution of δ in this particular case. Note that due to the complex construction of the PIGLET matrices, we are not able to reach full convergence for this method as discussed before for the energetic properties.

Despite this general observation, we would like to point

out that in particular at the ultra-low temperature of 1.67 K, using either PIGLET or PIQTB leads to an improvement of one order of magnitude on the deviation $d(\rho_P, \rho)$ of the proton transfer coordinate w.r.t. its converged distribution over standard PILE simulations in the small P limit.

In conclusion, both the PIQTB and PIGLET methods are able to accelerate the convergence of most structural properties, although one needs to be careful when studying highly anharmonic properties such as the proton sharing coordinate which relates to an intermolecular distance.

C. Nuclear Delocalization Properties

Having confirmed that colored noise thermostats are able to accelerate the convergence of both, energies and structural properties even down to ultra-low temperatures, we now investigate the effect of these thermostats on the delocalization of the nuclei. The nuclear delocalization is directly related to the fluctuations of the position operator

$$\sigma^2 = \frac{1}{P} \sum_{s=1}^P \langle (\mathbf{r}_s - \langle \mathbf{r}_s \rangle)^2 \rangle \quad (8)$$

which, in the path integral framework, can be decomposed into two additive contributions,⁶⁷

$$\sigma^2 = \sigma_c^2 + r_g^2, \quad (9)$$

where the first term is the fluctuations of the centroid of the ring polymer $\mathbf{r}_c = \sum_{s=1}^P \mathbf{r}_s / P$ which contains the thermal fluctuations. The second term is the squared radius of gyration,

$$r_g^2 = \frac{1}{P} \sum_{s=1}^P \langle (\mathbf{r}_s - \mathbf{r}_c)^2 \rangle, \quad (10)$$

that quantifies the spread of the ring polymer and, thus, is a direct measure of the quantum delocalization at the given temperature.

While the energetic and structural properties both showed only small changes when decreasing the temperature, quantum delocalization increases significantly when T decreases. For example, the radius of gyration of the dangling hydrogens is increasing from $r_g \approx 0.2 \text{ \AA}$ at 100 K to $r_g \approx 0.9 \text{ \AA}$ at 1.67 K. It has recently been shown that the PIGLET method can exhibit a very slow Trotter convergence of r_g at low temperatures and that it can even become difficult to converge this quantity at ultra-low temperatures.³¹ We thus verify that the PIGLET and PIQTB methods are able to converge towards the correct value of the radius of gyration. The dependence of the radius of gyration on the number of path integral replicas using the three different thermostating approaches is depicted in Fig. 3 for 1.67 K; the convergence at the

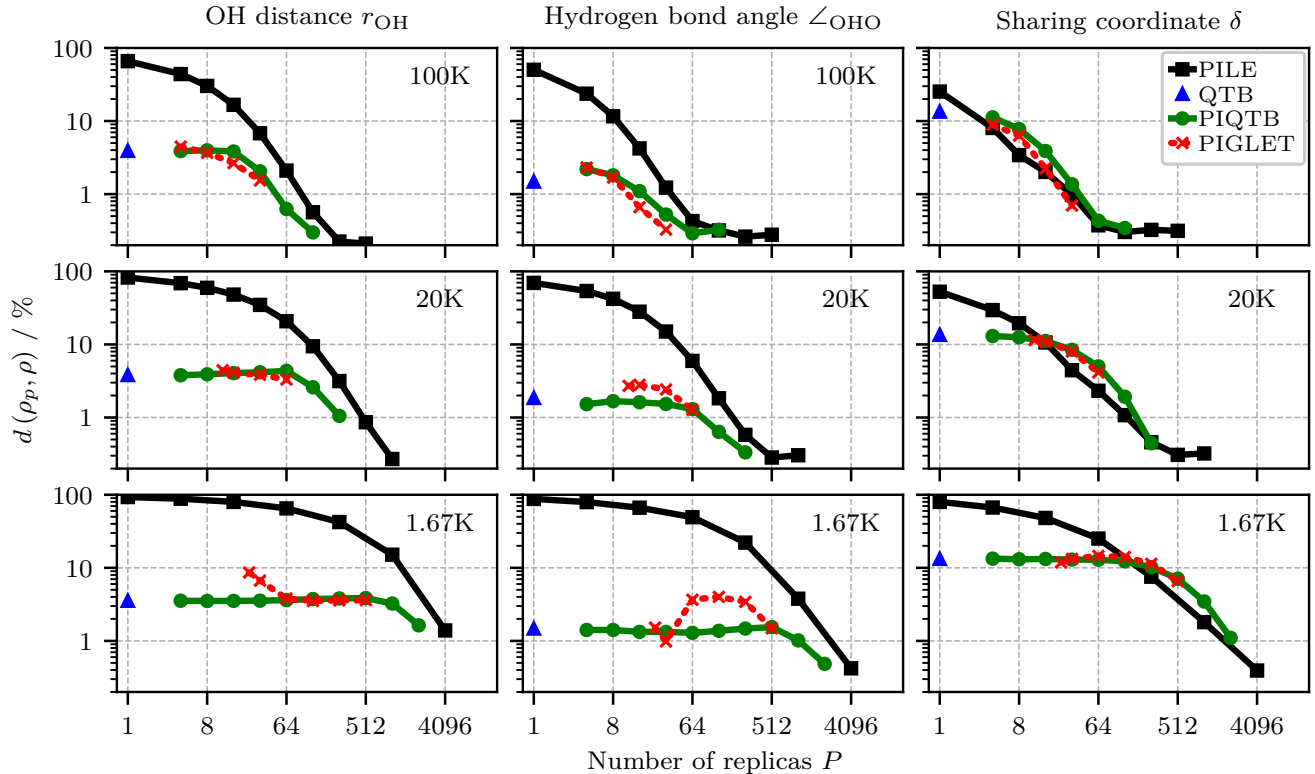


Figure 2. Convergence of the distribution functions of r_{OH} distances (left column), the \angle_{OHO} angle (center column) and of the proton sharing (transfer) coordinate δ (right column) of the Zundel cation, H_5O_2^+ , with respect to the number of replicas P at $T = 100, 20$ and 1.67K as obtained using the PILE (black squares), PIGLET (red crosses) and PIQTB (green circles) thermostats. The blue triangles show the results obtained with the bare QTB ($P = 1$) thermostat. The measure of convergence as a function of P is defined in Eq. (7). Note that the statistical error bars are smaller than the symbol size in all shown cases.

other two temperatures is similar and can be found in the Supporting Information. We first note that, compared to the convergence of all the other quantities studied here, the convergence of r_g is surprisingly fast with the PILE thermostat. Indeed, at 1.67K convergence is reached roughly at $P \approx 256$ replicas for all nuclei in the system. Both, PIGLET and PIQTB converge towards the correct value of r_g , however the convergence is rather slow and the required number of beads is approximately the same as for the PILE thermostat. It is also worth mentioning that the PIQTB and PIGLET methods approach the converged value from above and, therefore, both methods tend to *overestimate* the delocalization – if the number of path integral replicas is *too small*. This overestimation for lower Trotter numbers is caused by transient exchange of the shared proton by one of the dangling hydrogen atoms for some of the beads that renders the unique separation into shared proton and dangling hydrogens impossible in this case. Note that the lowest normal mode frequencies that are directly related to the evolution of the radius of gyration evolve rather slowly at ultra-low temperatures. This leads to some minor statistical fluctuations visible in Fig. 3 although every simulation was propagated for 0.5 ns . Overall, these results clearly prove

that colored noise thermostats do describe the quantum delocalization of the nuclei correctly when using a sufficiently large number of replica, however without any major acceleration compared to standard PIMD.

D. Anisotropic Shape of the Hydrogen-bonded Proton

After having established that colored noise thermostatting methods are able to correctly describe energetic, structural and delocalization properties of the Zundel cation down to ultra-low temperatures, we can use this system as a probe for different hydrogen-bonding situations to draw some more general conclusions. For this purpose it is important to note that the proton transfer barrier in the Zundel cation is well-known⁶⁸ to feature a very strong dependence on the oxygen-oxygen distance r_{OO} . More interestingly, the anisotropy of the nuclear quantum delocalization of such shared protons has been shown⁶⁹ to be strongly dependent on the hydrogen bond length. Fig. 4 (top) depicts cuts through the Coupled Cluster PES along the proton sharing coordinate δ for different donor-acceptor distances. For short distances, the potential energy profile is characterized by a single

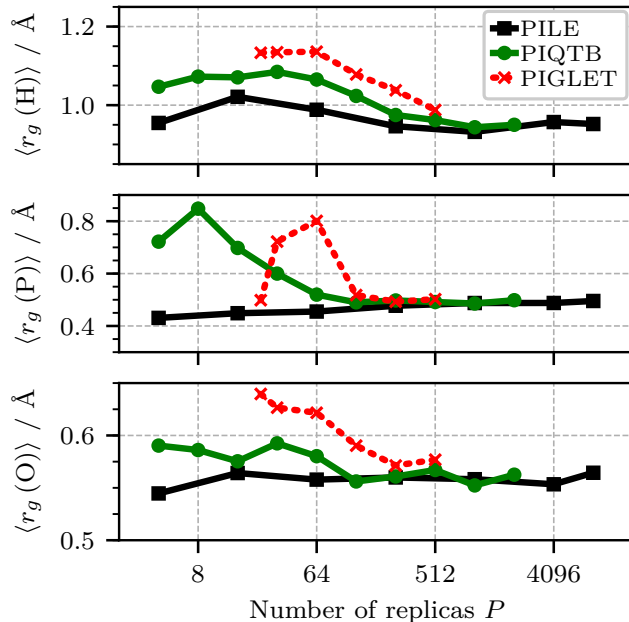


Figure 3. Convergence of the radius of gyration $\langle r_g \rangle$ of the Zundel cation, H_5O_2^+ , with respect to the number of replicas P for the dangling hydrogen atoms (top), the shared proton (middle) and the oxygen atoms (bottom) at 1.67K as obtained using the PILE (black squares), PIGLET (red crosses) and PIQTB (green circles) thermostats.

well centered around the midpoint of the O-O distance. Increasing r_{OO} leads to the appearance and growth of a centered barrier that separates two energetically equivalent proton positions, so that the energy profile for proton transfer becomes a double well potential. This typical dependence is encountered in almost every hydrogen bond, although asymmetric environments typically lift the perfect degeneracy of the two minima. We can exploit this to use the Zundel cation as a prototypical model of different hydrogen-bonding situations by imposing a specific O-O distance, mimicking strong and weak hydrogen bonds in case of short and long donor-acceptor distances. Indeed, the associated distribution of the proton sharing coordinate δ at 100 K for different restrained values of r_{OO} shown in Fig. 4 (bottom) demonstrates that we can describe fully centered up to very asymmetric hydrogen-bonding situations with this approach.

In the following, we assess in detail if colored noise thermostats are able to describe correctly the expected anisotropy of the nuclear quantum delocalization of the shared proton⁶⁹ for different values of the oxygen-oxygen distance in H_5O_2^+ . This is achieved in practice by restraining the oxygen atoms by two external harmonic potentials each acting on one oxygen atom such that the quantum expectation value of r_{OO} , i.e. $\langle r_{\text{OO}} \rangle$, remains close to the preset target value while the O-O distance still exhibits some fluctuations; see Sec. III for implementation details. This was done for all three temperatures

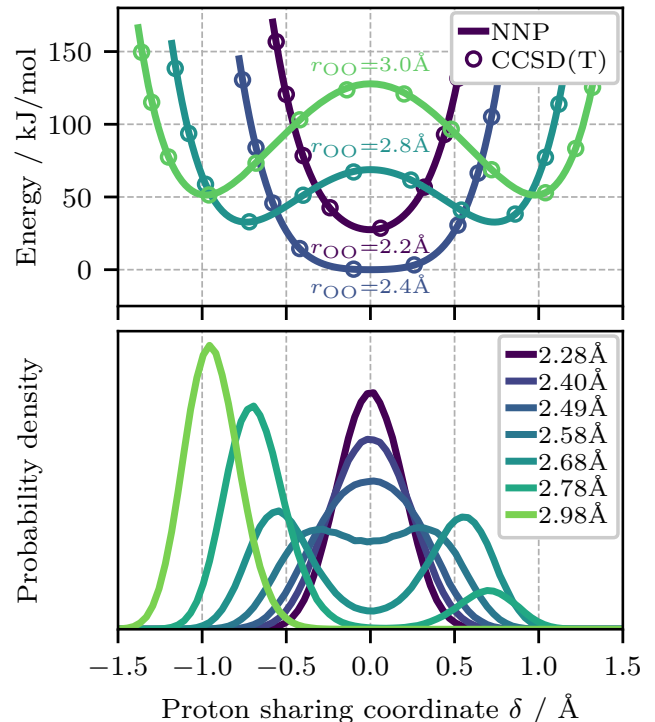


Figure 4. Top: Potential energy profile of the Zundel cation, H_5O_2^+ , along the proton sharing (transfer) coordinate δ with the oxygen distance r_{OO} constrained at different values (see text). The line is the energy profile obtained with the Neural Network Potential (NNP) and the open circles show the energy as directly obtained from the CCSD(T*)-F12a/AVTZ Coupled Cluster electronic structure calculations; the energies are reported relative to the equilibrium structure of H_5O_2^+ and the vertical offset is thus the shift of the potential energy surface due to constraining the donor-acceptor distance using the reported r_{OO} value. Bottom: Associated distribution functions of the δ coordinate at 100 K obtained using PILE simulations with $P = 1024$ beads (not symmetrized, see text for simulation protocol and sampling statistics) and r_{OO} restrained (see Sec. III for details) so that the average oxygen-oxygen distance $\langle r_{\text{OO}} \rangle$ (which is reported in the legend) remains close to the target value.

and all thermostating methods at nine different O-O distances varying from 2.25 up to 3.0 \AA , thus allowing us to probe the different proton transfer barriers shown in Fig. 4 including the barrierless limit. In the subsequent analysis we particularly focus on the anisotropy of the nuclear quantum delocalization of the shared proton in these various simulations. This is achieved by calculating the quantum expectation value of the gyration tensor

$$I_{\text{g}}^{\alpha,\beta} = \left\langle \frac{1}{P} \sum_{s=1}^P (\mathbf{r}_s^\alpha - \mathbf{r}_c^\alpha) \cdot (\mathbf{r}_s^\beta - \mathbf{r}_c^\beta) \right\rangle, \quad (11)$$

where $\mathbf{r}_s^{\alpha/\beta}$ and $\mathbf{r}_c^{\alpha/\beta}$ are the components of the position of the bead s and of the centroid of the ring polymer

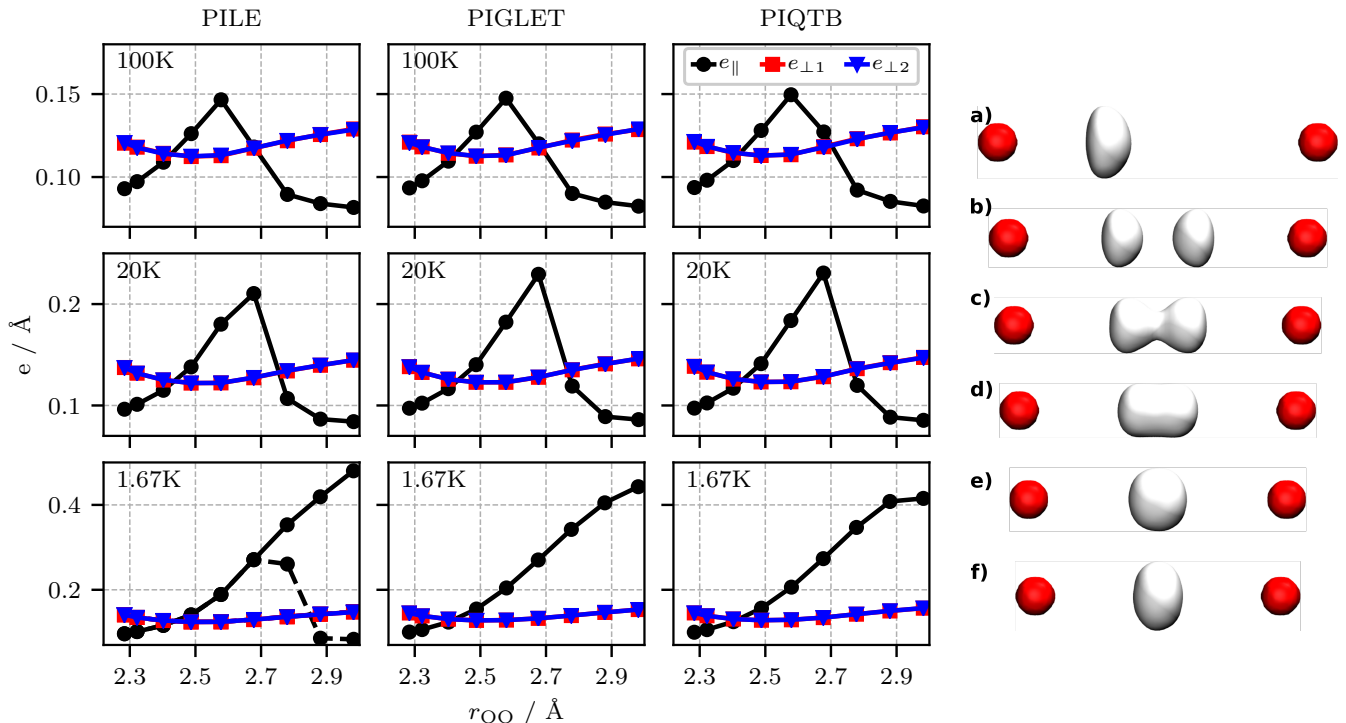


Figure 5. Left: Anisotropic nuclear quantum delocalization of the shared proton in the Zundel cation, H_5O_2^+ , given by the extent of the ellipsoid along the eigenvectors $e_{\parallel}, e_{\perp 1}, e_{\perp 2}$ of the gyration tensor as defined in Eq. (11) as a function of the oxygen-oxygen atom distance from restrained simulations using the PILE (left column), PIGLET (middle column) and PIQTB (right column) thermostats. The eigenvalues have been ordered such that the corresponding eigenvector of e_{\parallel} is oriented along the O-O vector, while the eigenvectors of $e_{\perp 1}$ and $e_{\perp 2}$ are orthogonal to the O-O vector; note that the latter two data sets are essentially on top of each other. Simulations at $T = 100, 20$ and 1.67 K using the PILE thermostat were performed with 1024, 2048 and 4096 beads, respectively, while PIQTB and PIGLET used 32, 128 and 512 replicas, respectively. The dashed line for the PILE results at 1.67 K is obtained from non-centered proton centroid simulations as described in the text. Right: Quantitative representation of the nuclear densities (a.k.a. spatial distribution functions, SDFs) of the shared proton (white) and the oxygen atoms (red) as a function of the O-O distance with a) 3.0 Å, b) 2.8 Å, c) 2.7 Å, d) 2.6 Å, e) 2.4 Å, f) 2.25 Å from PILE simulations at 20 K.

associated with the shared proton, respectively (where $\alpha, \beta = x, y, z$).

Next, by diagonalizing the $I_g^{\alpha, \beta}$ matrix one can extract quantitative information on the anisotropy of the nuclear quantum delocalization and thus on the general shape of the proton in the different hydrogen-bonding situations. The square root of the eigenvalues can be interpreted as the extent of the nuclear quantum delocalization in the direction of the corresponding eigenvector. We chose to order these eigenvalues according to the orientation of the corresponding eigenvector with respect to the O-O vector. The first eigenvalue e_{\parallel} is always oriented along the O-O vector, while $e_{\perp 1}$ and $e_{\perp 2}$ are orthogonal to it. As previously established⁶⁹ using a very similar analysis based on the inertia tensor, protons in hydrogen bonds can exhibit three distinct shapes depending on the average donor-acceptor distance. If $e_{\parallel} > e_{\perp 1} \approx e_{\perp 2}$, the proton has a “cigar-like” shape (see density d on the right side of Fig. 5), while for $e_{\perp 1} \approx e_{\perp 2} > e_{\parallel}$ a disk is formed (distribution a or f) whereas if $e_{\parallel} \approx e_{\perp 1} \approx e_{\perp 2}$ the shape

of the proton resembles a sphere (density e).

The dependence of these eigenvalues on the oxygen-oxygen distance for the three temperatures and the different thermostats under study is depicted in Fig. 5, where the bead numbers for the different thermostating methods were selected as specified in the caption according to convergence study from the previous section. Let us start by discussing the results obtained at the highest temperature, 100 K. The eigenvalues of the gyration tensor reveal that for strong compression, *i.e.* in the limit of extremely strong hydrogen bonds and thus very short O-O distances (2.25 to 2.3 Å), the proton adopts a disk-like shape in the central position between the two oxygen atoms indicating that it is “squeezed” between the two heavy atoms (see density f on the right side of Fig. 5). At 2.4 Å, the shape of the proton is more spherical (corresponding density e) before becoming cigar-like from 2.5 Å to 2.6 Å, thus spreading along the O-O vector (see density d). For these distances, the proton transfer barrier is first absent and then appears but remains small, so that the transfer

happens essentially as if no barrier was present. In the latter case, centering of the hydrogen bond takes place in a double well potential due to zero-point motion (as relevant, for instance, on the way of molecular ice VIII to ionic ice X as a result of applying extreme hydrostatic pressures⁷⁰). Since the potential becomes wider upon increasing r_{OO} , the nuclear wavefunction of the proton can stretch out in the direction of the oxygen atoms which at some point is assisted by tunneling over the emerging barrier. At an O-O separation of 2.7 Å, the barrier is high enough that only thermal proton hopping is present at 100 K (*i.e.* only hopping of the whole ring polymer is observed rather than the polymer being located simultaneously in both wells which would herald proton tunneling in hydrogen bonds⁷¹). This results again in a spherical shape, since the proton is now mainly located closer to either O₁ or O₂ but does not spread over the two wells. For larger distances, however, the shape finally evolves into being disk-like again. As the barrier height is increasing, the proton now stays trapped in one of two wells (*i.e.* no proton transfer events are observed during the whole simulation given the finite sampling time of 0.5 ns). The emergence of the disk-like shape can be understood by the decreasing attraction towards the opposite oxygen atom that leads to a larger extent of the nuclear wavefunction along the direction perpendicular to the O-O vector. This dependence of the proton shape on the oxygen-oxygen distance is additionally visualized in Fig. 5 (right) where also the nuclear densities of the oxygen atoms are depicted to scale with that of the proton. One-to-one comparison to the colored noise thermostats demonstrates that these 100 K PILE results, all the way from ultra-strong to very weak hydrogen-bonding, are rather well reproduced by both, PIGLET and PIQTB approaches using only a fraction of the number of beads.

Let us next focus on the temperature dependence of these properties. At 20 K the general trends described for 100 K remain unchanged however, the O-O region where the proton adapts a cigar-like shape is now extended up to 2.7 Å. In addition, the extent of the delocalization especially in the direction parallel to the O-O vector increases and has its maximum at 2.7 Å. This is due to an increase of the tunneling contribution to the proton transfer upon lowering the temperature that counteracts the decrease of thermal fluctuations. In practice, here we go from a mainly thermally activated proton transfer scenario at $T = 100$ K to a regime where tunneling is the dominating process at $T = 20$ K (*i.e.* the ring polymer is spreading over the two wells rather than hopping as a compact ball from one well to the other as observed upon thermal activation) for this specific O-O separation. Again, both PIGLET and PIQTB are able to reproduce the PILE results, however slightly overestimating the delocalization of the wavefunction along the hydrogen bond, $e_{||}$, for 2.7 Å.

Upon lowering the temperature further one expects that the tunneling contribution increases even more. Due to the degeneracy of the two minima of the double well

potential, the ground state wavefunction is required to be symmetric with respect to the center of the O-O distance and we should thus always obtain some tunneling contributions (even if very small when the barrier width and height are large). At ultra-low temperatures one should therefore expect that the region with a cigar-like proton shape, being associated with tunneling, further expands towards larger O-O distances. This is exactly what is observed for PIGLET and PIQTB at 1.67 K where we obtain a cigar-like shape of the proton even at donor-acceptor distances as large as 3.0 Å. In practice, however, the proton can still be trapped on one side of the molecule, due to non-ergodic sampling of the path integral, if the barrier is too high. This effect can be seen for the PILE results at 1.67 K in Fig. 5 (dashed lines), where the proton has been initialized closer to one of the oxygen atoms according to our standard protocol. Even within our simulation length of 0.5 ns we are not able to build up significant tunneling contributions for 2.9 and 3.0 Å and only partial tunneling is observed at 2.8 Å when using the PILE thermostat. As already mentioned for the radius of gyration, at such ultra-low temperatures, the lowest normal mode frequencies of the ring polymer are very important for the correct description of delocalization and tunneling. Since these modes evolve rather slowly, we see non-ergodic trapping of the proton at one side of the molecule for the PILE simulations at 1.67 K and O-O distances larger than 2.8 Å. However, if we initialize the proton in our simulations in the central position between the oxygen atoms and additionally restrain the centroid position to stay around the center of the O-O vector by a very soft harmonic potential being 25 000 times weaker than the external harmonic potentials acting on the oxygen atoms (providing the solid line for PILE at 1.67 K in Fig. 5), we can enforce a symmetric distribution. By doing so, we are able to obtain the same dependence of the eigenvalues of the gyration tensor as a function of the O-O distance for PILE as observed for PIGLET and PIQTB. This analysis reveals that the colored noise thermostating schemes tend to overestimate the tunneling contribution at these temperatures. However, due to inefficient sampling, standard PIMD simulations such as PILE have a tendency to underestimate these contributions especially at ultra-low temperatures and large O-O distances.

In summary, we showed that the anisotropic shape of the proton in the Zundel cation depends exquisitely on the donor-acceptor distance and thus on hydrogen bond length and, moreover, features exactly the same dependence as discovered in Ref. 69 for ice at different pressures. As expected, the tunneling regime that is corresponding to a cigar-like shape of the proton extends towards larger O-O separations, if the temperature is lowered. In addition, this anisotropy of the shape of the proton in hydrogen-bonded system is correctly reproduced by both PIGLET and PIQTB even down to ultra-low temperatures.

V. CONCLUSIONS AND OUTLOOK

In conclusion, we have shown that two modern colored noise thermostating methods that have been devised to accelerate path integral sampling using molecular dynamics techniques, namely PIGLET and PIQTB, are able to speed up the convergence of energetic and structural properties of the Zundel cation, H_5O_2^+ , even down to ultra-low temperatures on the order of one Kelvin, although highly anharmonic properties such as the proton sharing coordinate need to be treated with care. Upon suitably restraining the oxygen-oxygen distance, and thus the length of the hydrogen bond, from very short to fairly long donor-acceptor distances, we are able to drive this prototypical system from ultra-strong to very weak hydrogen-bonding scenarios. The latter are known to lead to greatly different nuclear quantum effects and thus delocalization as well as tunneling properties of the shared proton depending on temperature. Using Behler’s Neural Network Potentials of essentially converged Coupled Cluster accuracy, CCSD(T*)-F12a/AVTZ, enables us to perform path integral simulations using the “gold standard” of quantum chemistry for describing the interactions of this hydrogen-bonded complex.

Both, PIGLET and PIQTB are shown to converge to the correct nuclear delocalization properties like the radius of gyration. Moreover, both methods are able to correctly reproduce the anisotropy of the shape of the shared proton in all possible hydrogen-bonding situations, although they slightly but systematically overestimate tunneling contributions. Overall, our results validate that the use of these colored noise thermostating methods can provide great advantage over standard PIMD simulations by reducing the Trotter number that is required for the desired level of quantum convergence.

Given the generic character of the studied hydrogen bond depending on its length and on temperature, we expect that our conclusions are valid much beyond the H_5O_2^+ complex and should therefore apply to nuclear quantum effects on hydrogen bonding in general. This includes, in particular, hydrogen-bonded systems at ultra-low temperatures as for example encountered in superfluid helium environments or in He-tagged molecular complexes.

ACKNOWLEDGMENTS

It gives us great pleasure to thank Harald Forbert and Felix Uhl for helpful discussions. This research is part of the Cluster of Excellence “RESOLV” (EXC 1069) funded by the *Deutsche Forschungsgemeinschaft*, DFG. C.S. acknowledges partial financial support from the *Stiftung des Deutschen Volkes* as well as from the *Verband der Chemischen Industrie*. The computational resources were provided by HPC@ZEMOS, HPC-RESOLV, BOVI-LAB@RUB, and RV-NRW.

SUPPORTING INFORMATION

See the supplementary material for additional details on the implementation of the PIQTB into CP2k and supporting analyses of structural and nuclear delocalization properties.

REFERENCES

- J. P. Toennies and A. F. Vilesov, *Annu. Rev. Phys. Chem.* **49**, 1 (1998).
- J. P. Toennies and A. F. Vilesov, *Angew. Chemie Int. Ed.* **43**, 2622 (2004).
- J. P. Toennies, *Mol. Phys.* **111**, 1879 (2013).
- M. Okumura, L. I. Yeh, J. D. Myers, and Y. T. Lee, *J. Chem. Phys.* **85**, 2328 (1986).
- J. Roithová, A. Gray, E. Andris, J. Jašík, and D. Gerlich, *Acc. Chem. Res.* **49**, 223 (2016).
- A. Gutberlet, G. Schwaab, Ö. Birer, M. Masia, A. Kaczmarek, H. Forbert, M. Havenith, and D. Marx, *Science* **324**, 1545 (2009).
- H. Forbert, M. Masia, A. Kaczmarek-Kedziera, N. N. Nair, and D. Marx, *J. Am. Chem. Soc.* **133**, 4062 (2011).
- C. T. Wolke, J. A. Fournier, L. C. Dzigan, M. R. Fagiani, T. T. Odbadrakh, H. Knorke, K. D. Jordan, A. B. McCoy, K. R. Asmies, and M. A. Johnson, *Science* **354**, 1131 (2016).
- D. J. E. Callaway and A. Rahman, *Phys. Rev. Lett.* **49**, 613 (1982).
- M. Parrinello and A. Rahman, *J. Chem. Phys.* **80**, 860 (1984).
- M. E. Tuckerman, *Statistical Mechanics: Theory and Molecular Simulation* (Oxford University Press, New York, 2010).
- R. P. Feynman and A. R. Hibbs, *Quantum Mechanics and Path Integrals* (McGraw-Hill, New York, 1965).
- D. Chandler and P. G. Wolynes, *J. Chem. Phys.* **74**, 4078 (1981).
- D. M. Ceperley, *Rev. Mod. Phys.* **67**, 279 (1995).
- M. Takahashi and M. Imada, *J. Phys. Soc. Jpn* **53**, 3765 (1984).
- X. Li and J. Q. Broughton, *J. Chem. Phys.* **86**, 5094 (1987).
- M. Suzuki, *Phys. Lett. A* **201**, 425 (1995).
- S. A. Chin, *Phys. Lett. A* **226**, 344 (1997).
- A. Pérez and M. E. Tuckerman, *J. Chem. Phys.* **135**, 064104 (2011).
- V. Kapil, J. Behler, and M. Ceriotti, *J. Chem. Phys.* **145**, 234103 (2016).
- E. L. Pollock and D. M. Ceperley, *Phys. Rev. B* **30**, 2555 (1984).
- T. E. Markland and D. E. Manolopoulos, *J. Chem. Phys.* **129**, 024105 (2008).
- O. Marsalek and T. E. Markland, *J. Chem. Phys.* **144**, 054112 (2016).
- C. John, T. Spura, S. Habershon, and T. D. Kühne, *Phys. Rev. E* **93**, 043305 (2016).
- X. Cheng, J. D. Herr, and R. P. Steele, *J. Chem. Theory Comput.* **12**, 1627 (2016).
- M. Ceriotti, D. E. Manolopoulos, and M. Parrinello, *J. Chem. Phys.* **134**, 084104 (2011).
- F. Briec, H. Dammak, and M. Hayoun, *J. Chem. Theory Comput.* **12**, 1351 (2016).
- S. Jang, S. Jang, and G. A. Voth, *J. Chem. Phys.* **115**, 7832 (2001).
- T. M. Yamamoto, *J. Chem. Phys.* **123**, 104101 (2005).
- I. Poltavsky and A. Tkatchenko, *Chem. Sci.* **7**, 1368 (2016).
- F. Uhl, D. Marx, and M. Ceriotti, *J. Chem. Phys.* **145**, 054101 (2016).
- M. Ceriotti and D. E. Manolopoulos, *Phys. Rev. Lett.* **109**, 100604 (2012).
- M. E. Tuckerman, D. Marx, M. L. Klein, and M. Parrinello, *Science* **275**, 817 (1997).
- T. Spura, H. Elgabarty, and T. D. Kühne, *Phys. Chem. Chem. Phys.* **17**, 14355 (2015).

- ³⁵M. Ceriotti, G. Bussi, and M. Parrinello, *Phys. Rev. Lett.* **103**, 030603 (2009).
- ³⁶H. Dammak, Y. Chalopin, M. Laroche, M. Hayoun, and J.-J. Greffet, *Phys. Rev. Lett.* **103**, 190601 (2009).
- ³⁷M. Ceriotti, G. Bussi, and M. Parrinello, *J. Chem. Theory Comput.* **6**, 1170 (2010).
- ³⁸M. Ceriotti, in *Computational Trends in Solvation and Transport in Liquids*, Vol. 28, edited by G. Sutmann, J. Grotendorst, G. Gompper, and D. Marx (Forschungszentrum Jülich GmbH, Jülich, 2015) p. 1.
- ³⁹M. Ceriotti, G. Bussi, and M. Parrinello, *Phys. Rev. Lett.* **102**, 020601 (2009).
- ⁴⁰M. Ceriotti and M. Parrinello, *Procedia Comput. Sci.* **1**, 1607 (2010), iCCS 2010.
- ⁴¹S. Ganeshan, R. Ramírez, and M. V. Fernández-Serra, *Phys. Rev. B* **87**, 134207 (2013).
- ⁴²R. Kubo, *Rep. Prog. Phys.* **29**, 255 (1966).
- ⁴³H. B. Callen and T. A. Welton, *Phys. Rev.* **83**, 34 (1951).
- ⁴⁴J.-L. Barrat and D. Rodney, *J. Stat. Phys.* **144**, 679 (2011).
- ⁴⁵M. Ceriotti, G. Miceli, A. Pietropaolo, D. Colognesi, A. Nale, M. Catti, M. Bernasconi, and M. Parrinello, *Phys. Rev. B* **82**, 174306 (2010).
- ⁴⁶A. A. Hassanali, J. Cuny, M. Ceriotti, C. J. Pickard, and M. Parrinello, *J. Am. Chem. Soc.* **134**, 8557 (2012).
- ⁴⁷H. Dammak, E. Antoshchenkova, M. Hayoun, and F. Finocchi, *J. Phys.: Cond. Matter* **24**, 435402 (2012).
- ⁴⁸F. Calvo, F. Y. Naumkin, and D. J. Wales, *Chem. Phys. Lett.* **551**, 38 (2012).
- ⁴⁹F. Calvo, N.-T. Van-Oanh, P. Parneix, and C. Falvo, *Phys. Chem. Chem. Phys.* **14**, 10503 (2012).
- ⁵⁰Y. Bronstein, P. Depondt, F. Finocchi, and A. M. Saitta, *Phys. Rev. B* **89**, 214101 (2014).
- ⁵¹Y. Bronstein, P. Depondt, L. E. Bove, R. Gaal, A. M. Saitta, and F. Finocchi, *Phys. Rev. B* **93**, 024104 (2016).
- ⁵²Y. Bronstein, P. Depondt, and F. Finocchi, *Eur. J. Mineral.* **29**, 385 (2017).
- ⁵³S. Schaack, U. Ranieri, P. Depondt, R. Gaal, W. F. Kuhs, A. Falenty, P. Gillet, F. Finocchi, and L. E. Bove, *J. Phys. Chem. C* **122**, 11159 (2018).
- ⁵⁴O. N. Bedoya-Martínez, J.-L. Barrat, and D. Rodney, *Phys. Rev. B* **89**, 014303 (2014).
- ⁵⁵J. Hernández-Rojas, F. Calvo, and E. G. Noya, *J. Chem. Theory Comput.* **11**, 861 (2015).
- ⁵⁶F. Briec, Y. Bronstein, H. Dammak, P. Depondt, F. Finocchi, and M. Hayoun, *J. Chem. Theory Comput.* **12**, 5688 (2016).
- ⁵⁷CP2k Developers Team, (2018).
- ⁵⁸J. Hutter, M. Iannuzzi, F. Schiffmann, and J. VandeVondele, *WIREs: Comput. Mol. Sci.* **4**, 15 (2014).
- ⁵⁹M. Ceriotti, M. Parrinello, T. E. Markland, and D. E. Manolopoulos, *J. Chem. Phys.* **133**, 124104 (2010).
- ⁶⁰T. D. Kühne, M. Krack, F. R. Mohamed, and M. Parrinello, *Phys. Rev. Lett.* **98**, 066401 (2007).
- ⁶¹J. Behler and M. Parrinello, *Phys. Rev. Lett.* **98**, 146401 (2007).
- ⁶²J. Behler, *Angew. Chemie Int. Ed.* **56**, 12828 (2017).
- ⁶³C. Schran, F. Uhl, J. Behler, and D. Marx, *J. Chem. Phys.* **148**, 102310 (2018).
- ⁶⁴S. Chmiela, H. E. Sauceda, K.-R. Müller, and A. Tkatchenko, *arXiv*, 1802.09238 (2018).
- ⁶⁵A. H. Barrozo and M. de Koning, *Phys. Rev. Lett.* **107**, 198901 (2011).
- ⁶⁶H. Dammak, M. Hayoun, Y. Chalopin, and J.-J. Greffet, *Phys. Rev. Lett.* **107**, 198902 (2011).
- ⁶⁷C. P. Herrero and R. Ramírez, *J. Chem. Phys.* **145**, 224701 (2016).
- ⁶⁸D. Marx, *ChemPhysChem* **7**, 1848; D. Addendum: Marx, *ChemPhysChem* **8**, 209.
- ⁶⁹M. Benoit and D. Marx, *ChemPhysChem* **6**, 1738 (2005).
- ⁷⁰M. Benoit, A. H. Romero, and D. Marx, *Phys. Rev. Lett.* **89**, 145501 (2002).
- ⁷¹M. E. Tuckerman and D. Marx, *Phys. Rev. Lett.* **86**, 4946 (2001).